ARTICLE

Highly Asymmetric Lamellar Nanostructures from Nanoparticle–Linear Hybrid Block Copolymers

Kodai Watanabe,[a] Satoshi Katsuhara,[a] Hiroaki Mamiya,[b] Yukihiko Kawamura,[c] Takuya Yamamoto,[d] Kenji Tajima,[d] Takuya Isono,[*d] Toshifumi Satoh[*d]

Received 00th January 20xx,
Accepted 00th January 20xx

DOI: 10.1039/x0xx00000x

Highly asymmetric lamellar (A-LAM) nanostructure is one of the most important template geometries for block copolymer (BCP) lithography. However, A-LAM is unattainable from conventional BCPs, and there is no general molecular design strategy for A-LAM-forming BCP. Herein, a nanoparticle–linear hybrid BCP system is reported, which is designed based on the intramolecular crosslinking technique, as a remarkably effective platform to obtain the A-LAM morphology. The hybrid BCPs consisting of polystyrene single-chain nanoparticles and linear polylactide segments show a remarkable capability to form the A-LAM morphology in bulk, where a maximum width ratio of 4.1 between the two domains is obtained. This unusual phase behavior is attributed to the bulky and rigid characteristics of the nanoparticle block. Furthermore, the thin films of these hybrid BCPs show perpendicularly oriented A-LAM morphology on a chemically modified Si substrate, allowing promising application in the fabrication of asymmetric line-and-space nanopatterns.

Introduction

Nanolithography is an important technique used to fabricate various components in the microelectronics industry, such as integrated circuits (ICs), quantum dots, and diffraction gratings. Although the development of conventional "top-down" photolithography has enabled the remarkable miniaturization of electronic devices, current advanced technologies (*e.g.*, extreme ultraviolet lithography and multiple patterning technique) are typically expensive and/or time-consuming.[1-3] As a breakthrough approach to resolve the above-mentioned monetary and time consumption issues, block copolymer (BCP) lithography using microphase-separated structures via directed self-assembly has attracted considerable research attention.[4-8] As small features (*i.e.*, < 10 nm) are needed to satisfy the ever increasing demand for the miniaturization and integration of IC chips, one practical measure is the decrease in the sizes of the microphase-separated structures. Therefore, many research groups have focused on developing the "high χ–low N BCPs", where χ represents the Flory-Huggins interaction parameter and N is the overall degree of polymerization, to create ultrafine self-assembled nanopatterns.[9-13] In addition, the control over structural orientation is important for BCP lithography because the lamellar (LAM) morphology, which is typically used as a lithographic template among various types of microphase-separated morphologies, should be perpendicularly oriented in the thin film with respect to the substrate to fabricate the desired line and space (L/S) structure on the underlying substrate.[14-18]

Although recent research has focused mainly on addressing the above-mentioned aspects, achieving nonclassical microphase-separated morphologies is also a key challenge that needs to be overcome to diversify the accessible pattern geometries using BCP lithography.[19,20] One important geometry, particularly for the logic IC design, is the asymmetric L/S structure, wherein the space width is much larger than the line width, which can potentially be obtained from a highly asymmetric LAM (A-LAM) nanostructure. However, as the morphology of the microphase-separated structure is mainly governed by the volume fractions of the two blocks, the formation of LAM morphology occurs only near the symmetric block composition (Figure 1a). This makes it challenging to obtain the A-LAM morphology of the two phases with significantly different widths. A few pioneering studies for the fabrication of A-LAM nanostructures have recently been reported, in which specific molecular designs and/or polymer blending techniques have been employed (Figure 1b).[21-23] Kim *et al.* demonstrated A-LAM formation through the binary blending of compositionally asymmetric A–B and A–C BCPs, in which the minority blocks (B and C) strongly interacted with each

[a]*Graduate School of Chemical Sciences and Engineering, Hokkaido University, Sapporo 060-8628, Japan*
[b]*Quantum Beam Unit, Advanced Key Technologies Division, National Institute for Materials Science (NIMS), Tsukuba 305-0047, Japan*
[c]*Neutron Science and Technology Center, Comprehensive Research Organization for Science and Society (CROSS), Tokai 319-1106, Japan*
[d]*Faculty of Engineering, Hokkaido University, Sapporo 060-8628, Japan*
[*]Address correspondence to satoh@eng.hokudai.ac.jp and isono.t@eng.hokudai.ac.jp
Electronic Supplementary Information (ESI) available: [details of any supplementary information available should be included here]. See DOI: 10.1039/x0xx00000x

other through hydrogen bonding.[21] In another study, Lynd *et al.* found that an A(BA)$_3$-type miktoarm star BCP could exhibit A-LAM morphology with an extremely high degree of asymmetry by blending with the A homopolymer.[22] However, these approaches are not versatile enough to be applied to other BCP systems because these are based on a specific non-covalent interaction or involve time-consuming synthesis. Conversely, Cheng *et al.* designed the BCPs consisting of multiple polyhedral oligomeric silsesquioxane (POSS) derivatives and a long linear polystyrene (POSS-based multiheaded BCPs).[23] Although they successfully obtained A-LAM morphologies because of the bulkiness of the POSS block, it is very difficult to achieve the necessary perpendicular orientation in the thin film because of the remarkably low surface free energy of the Si-containing segment.[24,25] Therefore, to further advance BCP lithography, the development of a novel strategy with versatility toward various types of BCPs to achieve an A-LAM morphology while affording a perpendicular orientation in the thin film is essential.

Considering the previously mentioned POSS-based multiheaded BCPs, one of the key parameters by which the A-LAM morphology is stabilized is the bulkiness of the minority block at the interface. Indeed, it is known that the LAM region in the phase diagram of AB$_n$-type miktoarm star BCPs is shifted toward the higher A-block composition because of the presence of the bulky B$_n$-block, resulting in A-LAM morphologies.[26] As a new alternative method to generate a bulky architecture, an intramolecular crosslinking technique is herein considered to create bulky and rigid single-chain polymer nanoparticles from linear pre-polymers bearing crosslinkable moieties.[27-33] For example, Meijer *et al.*[34] and Pomposo *et al.*[35] observed globule-like formations of the resulting crosslinked nanoparticles using microscopy, which were further confirmed by the small angle X-ray scattering (SAXS) measurements in solution and molecular dynamics simulations. Therefore, these previous studies allowed us to hypothesize that intramolecularly crosslinked nanoparticles could be promising candidates as the minority blocks of BCPs to achieve A-LAM morphologies.

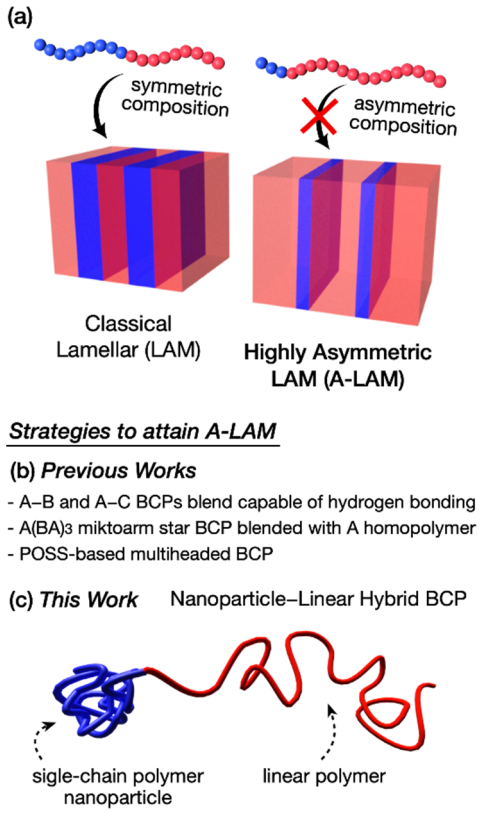

Figure 1. (a) Schematic representation of the classical LAM and A-LAM morphologies. Strategies involved in the (b) previous and (c) this work to obtain A-LAM morphology.

According to the above hypothesis, highly asymmetric BCPs consisting of an intramolecularly crosslinked segment as the minority block and a longer linear segment as the majority block, herein referred to as "nanoparticle–linear hybrid BCPs" were fabricated (Figure 1c). Previously, we established a Ru-catalyzed intramolecular olefin metathesis reaction that was tolerant of a wide range of pre-polymers possessing double bonds on the side-chain, owing to the high reactivity and excellent functional group tolerance of the Grubbs' catalyst.[36-38] The current strategy therefore applies the intramolecular olefin metathesis reaction to a perpendicular LAM-forming BCP to fulfill the requirements discussed above. An established BCP system, polystyrene-*b*-poly(*rac*-lactide) (PS-*b*-PLA), was employed because it afforded some important advantages including high segregation strength between the two blocks to achieve small domain sizes[39] and ability to form a perpendicularly oriented LAM in the thin film when employing an appropriate underlayer.[40] Therefore, the BCPs consisting of intramolecularly crosslinked poly[styrene-*st*-(*p*-3-butenyl styrene)] and linear poly(*rac*-lactide) (*i.e.*, SBS(*cl*)–LA) with not only an asymmetric composition but also symmetric composition were synthesized to elucidate the self-assembly behavior of the nanoparticle–linear hybrid BCPs. Well-ordered A-LAM morphologies were created in the bulk state from the asymmetric BCPs, whereas a double gyroid structure was formed from the symmetric BCPs. Importantly, the perpendicularly oriented A-LAM morphologies could be successfully prepared on a chemically modified Si substrate, demonstrating the promising potential of BCP lithography applications.

Results

Synthesis of Nanoparticle–Linear Hybrid Block Copolymers

The initial effort was directed toward the synthesis of a series of BCPs consisting of an intramolecularly crosslinked poly[styrene-*stat*-(*p*-3-butenyl styrene)] and linear poly(*rac*-lactide) (*i.e.*, P(S-*stat*-BS)(*cl*)-*b*-PLAs (SBS(*cl*)–LA)). In a previous study, we established a synthetic pathway for nanoparticle–linear hybrid BCPs, which involved the preparation of a linear–linear BCP and subsequent intramolecular crosslinking of one of the blocks.[38] However, such a pathway can cause variations in the degree of

crosslinking among the samples with varied PLA chain lengths. To prevent any potential effects of structural variations on the resulting morphology due to intramolecular crosslinking, an alternative approach to nanoparticle–linear hybrid BCP formation has been developed herein, as shown in Figure 2. Initially, the SBS(*cl*) block is prepared, and then the PLA chain is extended from the hydroxyl chain end of the SBS(*cl*) (detailed procedures are described in the Supporting Information). By employing a common SBS(*cl*), a series of SBS(*cl*)–LAs with varied PLA chain lengths can be synthesized, while maintaining the same molecular weight and degree of crosslinking of the SBS(*cl*) block, thus allowing the investigation of the effects of the PLA chain length on the resulting morphology.

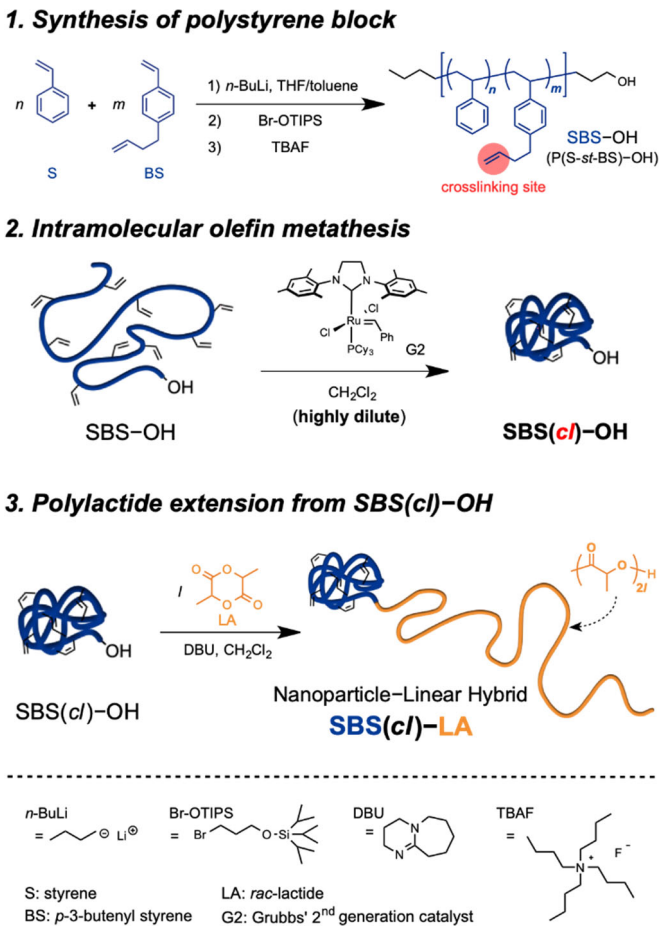

Figure 2. Preparation of nanoparticle–linear hybrid SBS(*cl*)–LA in three steps.

First, the hydroxyl-terminated P(S-*stat*-BS)s with varied molecular weights (MWs) and BS mole fractions (f_{BS}s) (*i.e.*, $S_{21}BS_8$–OH (M_n = 3,600, $Đ$ = 1.08, f_{BS} = 0.29), $S_{33}BS_{14}$–OH (M_n = 5,760, $Đ$ = 1.04, f_{BS} = 0.30), $S_{65}BS_{28}$–OH (M_n = 11,100, $Đ$ = 1.04, f_{BS} = 0.30), and $S_{47}BS_{47}$–OH (M_n = 12,400, $Đ$ = 1.04, f_{BS} = 0.50)) were prepared, wherein the subscript numbers denote the degree of polymerization (DP) of each monomer. Notably, $S_{65}BS_{28}$–OH and $S_{47}BS_{47}$–OH were designed to be different in f_{BS} values but comparable in DP, which allowed the determination of the effect of crosslink density on the microphase separation behavior. The obtained SBS–OHs were then subjected to intramolecular olefin metathesis reaction using Grubbs' 2nd generation catalyst (G2) ($[SBS–OH]_0$ = 0.30 g L^{-1}, $[G2]_0/[BS\ unit]_0$ = 0.01), affording the corresponding hydroxyl terminated intramolecularly crosslinked SBS–OHs (SBS(*cl*)–OHs) with an olefin conversion of ≥85% (Table S1: ^{1}H NMR spectra, size exclusion chromatography (SEC) traces, and infrared spectra are shown in Figures S1–S9). The differential scanning calorimetry (DSC) captured the increase in the glass transition temperatures (T_gs) after the crosslinking, which also confirmed the formation of the intramolecularly crosslinked structures (Figure S10).[36,38] Although the T_g of $S_{47}BS_{47}$(*cl*)–OH could not be clearly observable in its DSC curve likely due to the significantly reduced chain mobility associated with the high degree of crosslinking,[41] the T_g should be much higher than those of other SBS(*cl*)–OHs. Subsequently, the ring-opening polymerization of the *rac*-lactide was performed using SBS(*cl*)–OHs as the macroinitiator to produce the nanoparticle–linear hybrid SBS(*cl*)–LAs, in which the weight fraction of the poly(*rac*-lactide) (PLA) block (F_{LA}) was systematically varied from 0.46 to 0.92 (^{1}H NMR spectra and SEC traces are shown in Figures S11–S18). Although the final products contain a small amount of the high molecular weight byproducts (see the SEC traces), the percentages of the minor peaks were found to be only less than 10% of the total. Thus, these byproducts should have little impact on the microphase separation behaviors.

Three series of SBS(*cl*)–LAs (*i.e.*, $S_{21}BS_8$(*cl*)–LAs, $S_{33}BS_{14}$(*cl*)–LAs, and $S_{65}BS_{28}$(*cl*)–LAs), representing the low-, middle-, and high-MW series, respectively, as well as $S_{47}BS_{47}$(*cl*)–LA_{484} with a higher crosslink density were successfully obtained. In addition, the linear–linear type $S_{65}BS_{28}$–LA_{67} ($M_{n,SBS}$ = 11,100, $M_{n,LA}$ = 9,660, F_{LA} = 0.47) and $S_{65}BS_{28}$–LA_{466} ($M_{n,SBS}$ = 11,100, $M_{n,LA}$ = 46,600, F_{LA} = 0.86) were synthesized via the PLA chain extension from the $S_{65}BS_{28}$–OH macroinitiator to compare the microphase separation behaviors between the nanoparticle–linear hybrid BCPs and their linear–linear counterparts (^{1}H NMR spectra and SEC traces are shown in Figure S19). The molecular characteristics of the studied BCPs are summarized in Table 1.

Microphase Separation Behavior in the Bulk State

To elucidate the microphase-separation behavior of the SBS(*cl*)–LAs, small-angle X-ray scattering (SAXS) analysis was performed on the bulk samples. Prior to the SAXS measurements, the samples were thermally annealed at 150 °C ($S_{21}BS_8$(*cl*)–LAs, $S_{33}BS_{14}$(*cl*)–LAs, and $S_{65}BS_{28}$(*cl*)–LAs) or 180 °C ($S_{47}BS_{47}$(*cl*)–LA_{484}), well above the T_g of the corresponding SBS(*cl*) blocks, for 1 h under vacuum. The thermogravimetric analysis for a selected BCP sample confirmed the sufficient thermal stability at the annealing temperature (Figure S20). The resulting morphological characteristics of all samples are summarized in Table 1.

The SAXS results of the low-MW $S_{21}BS_8$(*cl*)–LA series confirm the morphological transition of the resulting

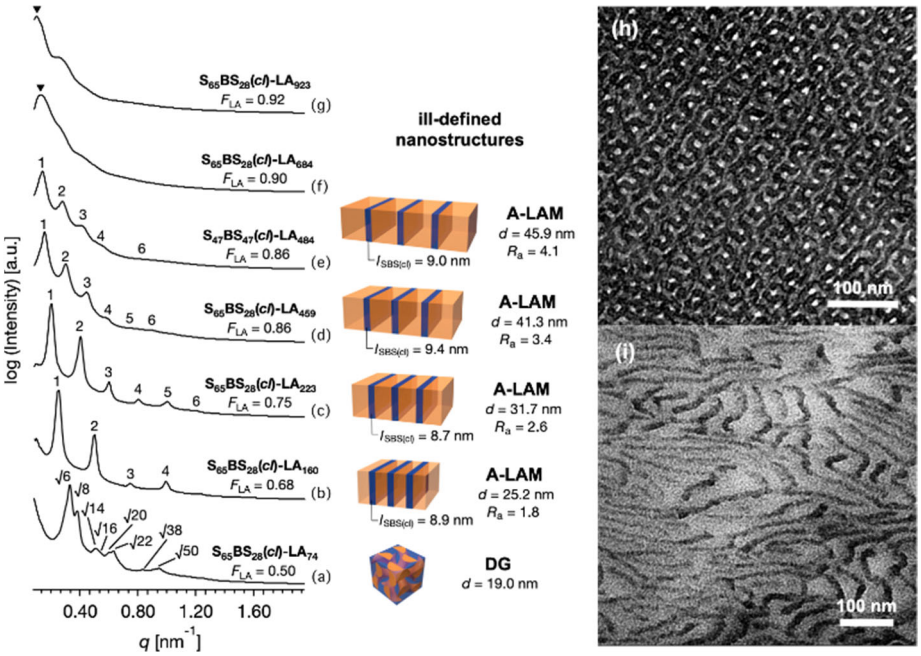

Figure 3. (a)-(g) SAXS profiles of $S_{65}BS_{28}(cl)$–LAs and $S_{47}BS_{47}(cl)$–LA_{484} with the corresponding schematic illustrations of each morphology (SBS(*cl*) and LA domains are shown in blue and yellow, respectively). TEM images of the microtomed (h) $S_{65}BS_{28}(cl)$–LA_{74} (DG, (211) plane) and (i) $S_{47}BS_{47}(cl)$–LA_{484} (A-LAM). Dark and bright domains correspond to the SBS(*cl*) and LA domains, respectively.

nanostructures with increasing F_{LA}. The SAXS profile of the lowest molecular weight $S_{21}BS_8(cl)$–LA_{20} (F_{LA} = 0.46) shows only a broad scattering peak corresponding to the disordered state, suggesting that the total DP of this BCP is insufficient to form an ordered nanostructure (Figure S21a). The SAXS profile of $S_{21}BS_8(cl)$–LA_{45} (F_{LA} = 0.65) exhibits a principal scattering peak at a q-value of 0.447 nm^{-1} (q^*) as well as higher-order scattering peaks at integer multiples of q^*, indicative of a LAM morphology (Figure S21b). The domain-spacing (d) of the microphase-separated structures can be calculated based on the relationship, $d = 2\pi/q^*$, which is 14.1 nm for this LAM structure. The SAXS profile of $S_{21}BS_8(cl)$–LA_{75} with a long PLA block (F_{LA} = 0.74) is also consistent with the LAM morphology (d = 16.7 nm) despite an asymmetric block composition (Figure S21c). $S_{21}BS_8(cl)$–LA_{115} with the longest PLA block (F_{LA} = 0.82) exhibits a hexagonally close-packed cylinder (HEX) morphology (d = 17.2 nm), as evident from the scattering peaks at the relative q-values of 1: √3: 2: √7: 3 in the SAXS profile (Figure S21d). The middle-MW $S_{33}BS_{14}(cl)$–LA series shows a similar trend: a morphological transition from LAM to HEX is observedupon increasing the F_{LA}, in which the LAM morphology is maintained up to an F_{LA} value of 0.74 (Figures S21f–h). Interestingly, the SAXS profile of the compositionally symmetric $S_{33}BS_{14}(cl)$–LA_{33} (F_{LA} = 0.46) exhibits multiple scattering peaks at relative q-values of √6: √8: √14: √16: √20: √22, which is in agreement with a highly ordered double gyroid (DG) morphology (Figures S21e).[42] When the molecular weight of the SBS(*cl*) block is further increased (high-MW $S_{65}BS_{28}(cl)$–LA series), the LAM region expands toward an even higher F_{LA}. Similar to the case of $S_{33}BS_{14}(cl)$–LA_{33}, the SAXS profile of the compositionally symmetric $S_{65}BS_{28}(cl)$–LA_{74} (F_{LA} = 0.50) exhibits a scattering pattern of the DG morphology (Figure 3a). Conversely, for the compositionally asymmetric BCPs (*i.e.*, $S_{65}BS_{28}(cl)$–LA_{160} (F_{LA} = 0.68), $S_{65}BS_{28}(cl)$–LA_{223} (F_{LA} = 0.75), and $S_{65}BS_{28}(cl)$–LA_{459} (F_{LA} = 0.86)), self-assembly into well-ordered LAM morphologies is supported by the appearance of more than four scattering peaks in the SAXS profiles (Figures 3b–d). The SAXS profile of $S_{47}BS_{47}(cl)$–LA_{484} (F_{LA} = 0.86) also exhibits a pattern associated with the LAM morphology (d = 45.9 nm; Figure 3e). Importantly, the morphologies of the microtomed samples of $S_{65}BS_{28}(cl)$–LA_{74} (DG) and $S_{47}BS_{47}(cl)$–LA_{484} (LAM) were visualized in the bulk using transmission electron microscopy (TEM). For $S_{65}BS_{28}(cl)$–LA_{74}, the typical pattern of the (211), (111), and (110) planes of DG morphology is clearly observed (Figures 3h, S22a, and S22b, respectively; the driving force of DG formation is also discussed in the Supplementary Information). The TEM image of $S_{47}BS_{47}(cl)$–LA_{484} shows a line pattern corresponding to the LAM morphology that consists of dark SBS(*cl*) and bright LA phases, where the domain widths are highly asymmetric (Figure 3i). Upon further increasing the F_{LA} values to 0.9 or higher, the well-defined morphology is no longer observed. Instead, the SAXS profiles of $S_{65}BS_{28}(cl)$–LA_{684} (F_{LA} = 0.90) and $S_{65}BS_{28}(cl)$–LA_{923} (F_{LA} = 0.92) exhibit broad primary scattering peaks (denoted with triangles) and weak higher-ordered peaks, indicative of the ill-defined nanostructures without any characteristic periodic structure (Figures 3f–g).

Based on all the above SAXS profiles except for $S_{47}BS_{47}(cl)$–LA_{484}, a phase diagram of the nanoparticle–linear hybrid BCP with respect to the F_{LA} and MW of the SBS(*cl*) block ($M_{n,SBS(cl)}$) was constructed (Figure 4). The previous data

for $S_{45}BS_{20}(cl)$–LA_{57} ($M_{n,SBS(cl)}$ = 7,710, $M_{n,LA}$ = 8,250, F_{LA} = 0.52, f_{BS} of linear prepolymer = 0.31) were also included as its molecular structure was expected to be almost identical to the samples prepared in this study.[38] As expected, the LAM window shifts toward the higher composition of the PLA block compared to that in the typical phase diagram of linear–linear BCPs, resulting in the A-LAM morphologies over a wide range of block compositions.

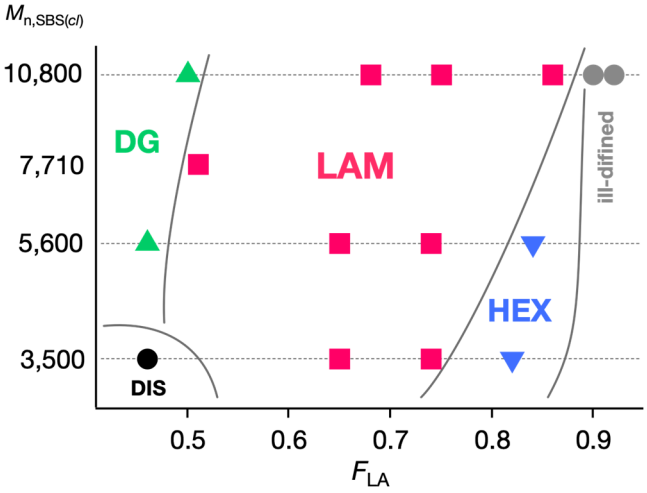

Figure 4. Experimentally constructed phase diagram for SBS(cl)–LAs. The points are plotted depending on F_{LA} and $M_{n,SBS(cl)}$. LAM (red squares), DG (green triangles), HEX (blue inverted triangles), and ill-defined (gray circles) morphologies are indicated. Black circle represents the disordered state. Gray lines indicate the phase boundary and numbers in parentheses represent the R_a values.

As the determination of the width of each domain in A-LAM is important for evaluating the degree of asymmetry, a correlation function analysis of the obtained SAXS profile, which has been widely employed for determining the layer thickness in the crystalline–amorphous lamellar structures of semi-crystalline polymers[43,44] and asymmetric lamellar microphase-separated morphologies,[23] was performed (details are included in the Supplementary Information; Figure S23). For the low-MW $S_{21}BS_8(cl)$–LA_{45} ($M_{n,SBS(cl)}$ = 3,500), the widths of the SBS(*cl*) and LA domains ($l_{SBS(cl)}$ and l_{LA}, respectively) are 5.3 nm and 8.8 nm, respectively, from which the asymmetric ratio (R_a = $l_{LA}/l_{SBS(cl)}$) is calculated as 1.7. To the best of our knowledge, the domain width of ~5 nm is the smallest among the LAM morphologies reported to date for a PS–PLA system. Arguably, a previous report indicates that the compositionally symmetric linear–linear PS–PLA with a PS block of ~3,500 g mol^{-1} is not capable of forming an ordered LAM structure (and produces the disordered state) due to an insufficient overall MW.[39] It is therefore noteworthy that obtaining such an exceptionally small LAM domain is clearly due to the ability of the nanoparticle–linear hybrid SBS(*cl*)–LA to form the A-LAM, wherein the long PLA chain contributes toward increasing the MW of the BCP, and thus exceeds the critical χN (referred to as the segregation strength). The same analysis was then applied to the middle-MW series to obtain domain widths and R_a values of the LAM morphologies, *i.e.*, R_a = 1.8 for $S_{33}BS_{14}(cl)$–LA_{72} ($l_{SBS(cl)}$ = 6.8 nm, l_{LA} = 11.9 nm) and R_a = 2.2 for $S_{33}BS_{14}(cl)$–LA_{112} ($l_{SBS(cl)}$ = 6.5 nm, l_{LA} = 14.1 nm), confirming the formation of A-LAM morphologies. However, the maximum F_{LA} value that allows the LAM formation is 0.74 for the low- and middle-MW series, which is comparable to that for the miktoarm star BCP system.[26]

Table 1. Molecular and morphological characteristics of SBS(*cl*)–LAs.

Sample Name	Molecular Characteristics				Morphological Characteristics				
	$M_{n,SBS(cl)}$[a]	$M_{n,LA}$[a]	F_{LA}[b]	$Đ$[c]	Morphology[d]	d[f] (nm)	$l_{SBS(cl)}$[g] (nm)	l_{LA}[g] (nm)	R_a[i]
$S_{21}BS_8(cl)$–LA_{20}	3,500	2,930	0.46	1.05	disorder	–	–	–	–
$S_{21}BS_8(cl)$–LA_{45}	3,500	6,550	0.65	1.04	A-LAM	14.1	5.3	8.8	1.7
$S_{21}BS_8(cl)$–LA_{70}	3,500	10,100	0.74	1.05	A-LAM	16.7	–[h]	–[h]	–
$S_{21}BS_8(cl)$–LA_{110}	3,500	15,900	0.82	1.03	HEX	17.2	–	–	–
$S_{33}BS_{14}(cl)$–LA_{33}	5,600	4,750	0.46	1.06	DG	13.0	–	–	–
$S_{33}BS_{14}(cl)$–LA_{72}	5,600	10,400	0.65	1.07	A-LAM	18.7	6.8	11.9	1.8
$S_{33}BS_{14}(cl)$–LA_{112}	5,600	16,200	0.74	1.06	A-LAM	20.6	6.5	14.1	2.2
$S_{33}BS_{14}(cl)$–LA_{201}	5,600	28,900	0.84	1.06	HEX	22.5	–	–	–
$S_{65}BS_{28}(cl)$–LA_{74}	10,800	10,700	0.50	1.09	DG	19.0	–	–	–
$S_{65}BS_{28}(cl)$–LA_{160}	10,800	23,000	0.68	1.06	A-LAM	25.2	8.9	16.3	1.8
$S_{65}BS_{28}(cl)$–LA_{223}	10,800	32,100	0.75	1.06	A-LAM	31.7	8.7	23.0	2.6
$S_{65}BS_{28}(cl)$–LA_{459}	10,800	66,100	0.86	1.09	A-LAM	41.3	9.4	31.9	3.4
$S_{65}BS_{28}(cl)$–LA_{684}	10,800	98,600	0.90	1.14	ill-defined	–	–	–	–
$S_{65}BS_{28}(cl)$–LA_{923}	10,800	133,000	0.92	1.10	ill-defined	–	–	–	–
$S_{47}BS_{47}(cl)$–LA_{484}	11,800	69,800	0.86	1.07	A-LAM[e]	45.9	9.0	36.9	4.1

[a]MW of the SBS(*cl*) block ($M_{n,SBS(cl)}$) and LA block ($M_{n,LA}$) determined using ^{1}H NMR spectroscopy ($CDCl_3$, 400 MHz). [b]Weight fraction of LA block calculated from $M_{n,LA}/(M_{n,SBS(cl)}+M_{n,LA})$. [c]Determined by SEC in THF using polystyrene standards. [d]Obtained after thermal annealing at 150 °C ([e]180 °C). [f]Determined by SAXS. [g]Determined from the correlation function analysis of SAXS profiles. [h]Not determined. [i]Asymmetric ratio of the LAM phases calculated from $l_{LA}/l_{SBS(cl)}$.

For the high-MW $S_{65}BS_{28}(cl)$–LA series with $M_{n,SBS(cl)}$ of 10,800, the formation of the A-LAM morphology is observed at an F_{LA} value of up to 0.86. Notably, the SAXS profile of the linear–linear type $S_{65}BS_{28}$–LA_{466} with an asymmetric composition (F_{LA} = 0.86) exhibits a scattering pattern consistent with the HEX morphology (Figure S24a). In addition, $S_{65}BS_{28}$–LA_{67} with a symmetric composition (F_{LA} = 0.47) also showed the HEX morphology (Figure S24b) whereas the crosslinked counterpart ($S_{65}BS_{28}(cl)$–LA_{67}, F_{LA} = 0.50) showed the DG one. These results clearly demonstrate that the unusual phase behavior of the nanoparticle–linear hybrid SBS(*cl*)–LAs is caused by the intramolecularly crosslinked SBS(*cl*) block. In contrast, the formation of the ill-defined nanostructures when F_{LA} > 0.90 is understandable because this region is positioned near the order–disorder boundary in the phase diagram. Considering that $S_{45}BS_{20}(cl)$–LA_{57} with F_{LA} of 0.52 exhibits the LAM morphology, the DG–LAM phase boundary of the high-MW $S_{65}BS_{28}(cl)$–LA series might exist at F_{LA} ≈ 0.5, resulting in a large LAM region with 0.5 < F_{LA} < 0.9. Such a wide region for possible LAM formation could not previously be achieved with the AB_n miktoarm BCP system, even when the branching number (*n*) was increased to 5,[26] demonstrating the remarkable capability of the nanoparticle–linear hybrid BCPs described herein to generate the A–LAM morphology. This phenomenon is attributed to a decrease in the interfacial curvature of the domain arising from the bulkiness and rigidity of the SBS(*cl*) block. It is unfavorable for the intramolecularly crosslinked nanoparticles to be packed into a curved microdomain, such as a cylinder or sphere, due to a large packing frustration, resulting in LAM morphologies with a less curved domain interface. Based on the correlation function analysis, the R_a values for $S_{65}BS_{28}(cl)$–LA_{160} ($l_{SBS(cl)}$ = 8.9 nm and l_{LA} = 16.3 nm), $S_{65}BS_{28}(cl)$–LA_{223} ($l_{SBS(cl)}$ = 8.7 nm and l_{LA} = 23.0 nm), and $S_{65}BS_{28}(cl)$–LA_{459} ($l_{SBS(cl)}$ = 9.4 nm and l_{LA} = 31.9 nm) are 1.8, 2.6, and 3.4, respectively, which reveal the highly asymmetric line patterns. Notably, the suppression of the third-ordered scattering peak in the SAXS profile of $S_{65}BS_{28}(cl)$–LA_{160} indicates that the width ratio between the two different phases is ~1:2 (Figure 3b),[45] which is consistent with the result of the correlation function analysis (R_a = 1.8). Interestingly, the $l_{SBS(cl)}$ values for the A-LAM morphologies are constant among each series (*i.e.*, ~6.5 nm and 9.0 nm for the middle-MW $S_{33}BS_{14}(cl)$–LA and high-MW $S_{65}BS_{28}(cl)$–LA series, respectively). This indicates that the $S_{65}BS_{28}(cl)$ blocks are packed in a similar manner in the narrow microdomains, regardless of the MW of the counter LA block. The packing model for the A-LAM morphologies is discussed in detail below.

Overall, the nanoparticle–linear hybrid BCPs self-assemble into the microphase-separated structures with completely different phase behaviors from that of the typical linear diblock copolymers. Remarkably, the upper limit of F_{LA} for LAM formation increases with an increase in the MW of the crosslinked nanoparticle block, eventually resulting in the unusual 0.5 < F_{LA} < 0.9 LAM region.

Chain Packing Model in A-LAM and Effect of Crosslink Density To clarify the driving force behind the formation of the unusual A-LAM morphologies, a chain packing model of the nanoparticle–linear hybrid BCPs based on the restrictions that did not affect the typical linear system was assumed. It is well-known that linear–linear BCPs with an asymmetric block composition are packed into a cone shape to minimize the interfacial energy and maximize the conformational entropy (Figure S25a). Importantly, the minority block chain must be stretched from its thermodynamically stable state to achieve a tapered cone-shaped packing because the chain volume must retain intact.[46] Upon the self-assembly of such cone-shaped molecules, a curved morphology (*e.g.*, HEX on BCC) can be formed. In contrast, it is difficult for the nanoparticle–linear hybrid BCPs with an asymmetric composition to be packed into a cone shape as the chain stretching of the nanoparticle block is restricted due to intramolecular crosslinking. As a result, the bulky nanoparticle block needs to be packed into a non-tapered space, resulting in the cylinder-shaped packing of the nanoparticle–linear hybrid BCP, which in turn self-assembles into a lamellar structure without any interfacial curvature (Figures 5a and S25b). As mentioned above, the widths of the SBS(*cl*) phases ($l_{SBS(cl)}$) for the three A-LAM morphologies

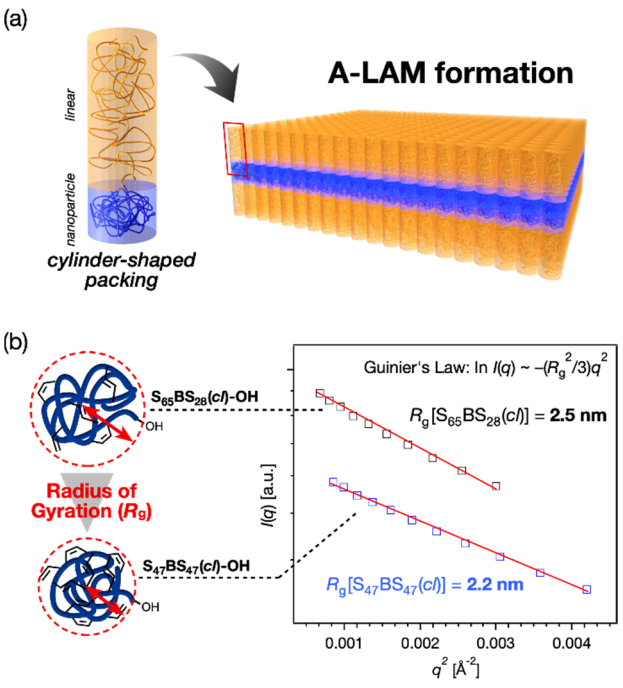

Figure 3. (a) Schematic of the cylinder-shaped packing of the nanoparticle–linear hybrid BCPs and their arrangement into the A-LAM morphology. (b) Guinier plots of the SANS data measured for $S_{65}BS_{28}(cl)$–OH (upper) and $S_{47}BS_{47}(cl)$–OH (lower). The R_g values are calculated based on the Guinier's law: ln $I(q)$ ~ $-(R_g^2/3)q^2$. The $I(q)$ data are vertically shifted by multiplying arbitrary constants.

formed by $S_{33}BS_{14}(cl)$–LAs and $S_{65}BS_{28}(cl)$–LAs are comparable among each series irrespective of the PLA chain length, which is consistent with the conformation of the nanoparticle segment that is nearly unchanged from its thermodynamically stable state.

With the assumed chain packing model in hand, the next step was to elucidate the effect of the SBS(*cl*) block crosslink density on A-LAM formation. Correlation function analysis of the $S_{47}BS_{47}(cl)$–LA_{484} (f_{BS} = 0.50, F_{LA} = 0.86) SAXS profile allowed the determination of the structural parameters of A-LAM ($l_{SBS(cl)}$ = 9.0 nm, l_{LA} = 36.9 nm, and R_a = 4.1), revealing a clear difference in the R_a value when compared to that of $S_{65}BS_{28}(cl)$–LA_{459} (f_{BS} = 0.30, F_{LA} = 0.86, R_a = 3.4), which likely stemmed from the difference in crosslink density because all other molecular characteristics of $S_{47}BS_{47}(cl)$–LA_{484} and $S_{65}BS_{28}(cl)$–LA_{459} were comparable. To further examine this issue, small-angle neutron scattering (SANS) measurements of $S_{65}BS_{28}(cl)$–OH and $S_{47}BS_{47}(cl)$–OH, as well as their linear precursors ($S_{65}BS_{28}$–OH and $S_{47}BS_{47}$–OH) in the bulk state (50% mixture in deuterated polystyrene with M_n of 8,800 g mol^{-1}) were obtained to identify their radius of gyration (R_g) values (details are included in the Supporting Information). Figure 5b shows the Guinier plots of the two SBS(*cl*)–OH samples obtained from the corresponding SANS profiles (Figure S26a). The R_g values of $S_{65}BS_{28}(cl)$–OH ($R_g[S_{65}BS_{28}(cl)]$) and $S_{47}BS_{47}(cl)$–OH ($R_g[S_{47}BS_{47}(cl)]$) are 2.5 and 2.2 nm, respectively, considering an approximation based on the Guinier law. The R_g values of the linear prepolymers are identical (2.9 nm, Figure S26b) because of the comparable *N* values, thus confirming that a high crosslink density results in a further reduction in R_g, which is consistent with our previous studies.[36,38] In addition, the R_g values of SBS–OHs (2.9 nm) are very close to that of the polystyrene with a DP of 93 in a theta solvent (2.7 nm, Supporting Information), supporting the reliability of the SANS analysis.[47] Using the above R_g values, the diameters ($2R_g$) of the SBS(*cl*) blocks are 5.0 nm and 4.4 nm, which coincide with the diameters of the cylinders packed with $S_{65}BS_{28}(cl)$–LA_{459} and $S_{47}BS_{47}(cl)$–LA_{484}, respectively. The difference in the cylinder packing diameters between the two BCPs likely results in a difference in the degree of stretching of the LA segments: the LA segment of $S_{47}BS_{47}(cl)$–LA_{484} should be packed into a cylinder with a smaller diameter, which forces the PLA chain to stretch more, leading to an increased l_{LA} in comparison to that of $S_{65}BS_{28}(cl)$–LA_{459}. Therefore, the crosslink density (*i.e.*, chain dimensions) of the nanoparticle segment acts as the driving force to alter the degree of stretching of the counter linear segment. A clear difference in the R_a values between $S_{65}BS_{28}(cl)$–LA_{459} and $S_{47}BS_{47}(cl)$–LA_{484} is thus observed because of this unique effect, wherein a maximum R_a of 4.1 is successfully obtained.

Microphase Separation Behavior in the Thin Film State

As control over the microdomain orientation in the thin films is important for pattern transfer to the underlying substrate in BCP lithography, the fabrication of the perpendicularly oriented A-LAM using $S_{65}BS_{28}(cl)$–LA_{160} and $S_{65}BS_{28}(cl)$–LA_{223} was examined.[48] Grazing incidence SAXS (GISAXS) was performed to evaluate the morphology and structural orientation inside the thin films. A polystyrene-*random*-poly(methyl methacrylate) (PS-*r*-PMMA) underlayer was applied to the Si substrate (details are included in the Supporting Information), which was demonstrated to yield perpendicular LAM morphologies in PS-*b*-PLA thin films.[40] The thin films were prepared via spin-coating the BCPs (0.66 wt% in toluene, 2000 rpm for 1 min) onto the chemically modified Si substrate, resulting in ~20-nm-thick films, which were then thermally annealed at 180 °C for 30 min. The 2D GISAXS pattern of the $S_{65}BS_{28}(cl)$–LA_{160} thin film exhibits intense Bragg rods (reflection stripes extending in the vertical direction) and second-order reflection spots along the in-plane direction, with relative scattering vector lengths from the specular reflection positions of 1 and 2, respectively, which strongly indicate the development of perpendicularly oriented LAM morphologies (Figure 6a-left). The analysis of the in-plane scattering profile extracted along the $2\vartheta_f$ direction at α_f = 0.116° affords a *d*-value of 24.7 nm, which is similar to the *d*-value in the bulk (25.2 nm; Figure S27a). The 2D GISAXS pattern of the $S_{65}BS_{28}(cl)$–LA_{223} thin film exhibits a similar diffraction pattern corresponding to the perpendicular A-LAM with a *d*-value of 29.9 nm (*d*-value in bulk = 31.7 nm; Figures 6b-left and S27b). Notably, considering that the above two patterns contain no diffraction spots in the out-of-plane directions, the LAM structures are perfectly perpendicular throughout the entire thin film depth.

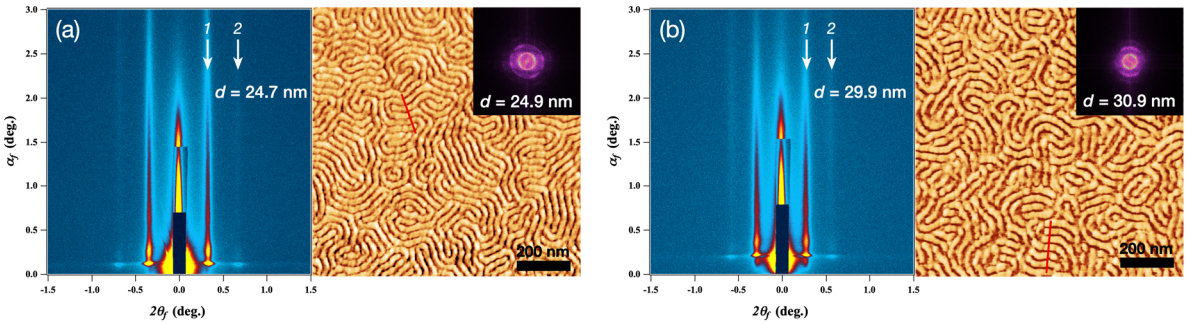

Figure 6. 2D GISAXS patterns (left) and AFM phase images (right) of (a) $S_{65}BS_{28}(cl)$–LA_{160} and (b) $S_{65}BS_{28}(cl)$–LA_{223} thin films on the PS-*r*-PMMA underlayer. The insets in the AFM images show the 2D FFT profiles.

Finally, the thin film surface morphologies were visualized using atomic force microscopy (AFM). The fingerprint patterns are clearly observed in the phase images of both the $S_{65}BS_{28}(cl)$–LA_{160} and $S_{65}BS_{28}(cl)$–LA_{223} thin films over a large area, revealing highly organized perpendicular LAM morphologies (Figures 6a-right, 6b-right**,** and S28). The *d*-values extracted from the 2D fast Fourier transform (FFT) profiles are 24.9 nm and 30.9 nm for $S_{65}BS_{28}(cl)$–LA_{160} and $S_{65}BS_{28}(cl)$–LA_{223}, respectively, which are in good agreement with those estimated from 2D GISAXS analysis. In particular, the line widths of the bright LA microdomains are larger than those of the dark SBS(*cl*) microdomains, which further supports the formation of A-LAM morphology in the thin film state. The highly-asymmetric patterns, especially for $S_{65}BS_{28}(cl)$–LA_{223}, can also be confirmed from the cross-sectional profiles extracted along with the red lines in the AFM phase images (Figure S29).

Overall, perpendicularly oriented A-LAMs are successfully obtained by combining a random copolymer underlayer with a simple thermal annealing process. This strongly indicates that the nanoparticle–linear hybrid BCPs are promising for application as a next-generation BCP lithography technique. Notably, selective one-domain removal, an essential step in the lithographic process, can be potentially achieved by either the wet- or dry-etching of the PLA domain using NaOH solution[49-51] or O_2 plasma,[52] respectively.

Conclusions

In summary, compositionally asymmetric nanoparticle–linear hybrid SBS(*cl*)–LAs with a long PLA block (F_{LA} ~ 0.92) are designed and their remarkable capability to form A-LAM morphology is demonstrated. According to the experimentally constructed phase diagram, the LAM window of the SBS(*cl*)–LAs includes a wide range of block compositions in the high F_{LA} regime (with maxima of $0.5 < F_{LA} < 0.9$), which arguably arises from the bulky and rigid conformation of the SBS(*cl*) block. A high crosslink density of the SBS(*cl*) block results in more stretching of the linear LA block in the A-LAM morphology, and a maximum R_a of 4.1 is successfully obtained. Notably, the widths of the minor SBS(*cl*) domains, corresponding to the line part of the L/S structure on the lithographic process, are <10 nm for all the studied MWs. Moreover, A-LAM morphologies with constant and varied widths of thin and thick domains, respectively, are successfully obtained, which is important for lithographic applications such as L/S design for a logic device that requires the space width to be controlled while maintaining the line width. Most importantly, the intensive thin film studies utilizing GISAXS and AFM demonstrate the capability of the SBS(*cl*)–LAs to produce a perpendicularly oriented A-LAM morphology on a silicon substrate with a random copolymer underlayer. Considering that the ruthenium-catalyzed olefin metathesis reaction shows an excellent functional group tolerance and its versatility has been previously demonstrated,[36] this strategy can be expanded to various BCP systems. The nanoparticle–linear hybrid BCP, which can be extended to the other BCP systems, can expand the accessible self-assembled morphologies, thus contributing to the technological advancement and innovation of BCP lithography as well as related nanomaterial sciences.

Conflicts of interest

There are no conflicts to declare.

Acknowledgements

This work was financially supported by the JSPS Grant-in-Aid for Research Activity Start-up (26888001, T.I.), Grant-in-Aid for Young Scientists (B) (15K17862, T.I.), Grant-in-Aid for Scientific Research (B) (19H02769, T.S.), and the Photo-excitonix Project (Hokkaido University, T.S.). K.W. was funded by a JSPS Fellowship for Young Scientists. T.I. gratefully acknowledges the Nanotech CUPAL NRP program. This work was, in part, performed under the approval of the Photon Factory Program Advisory Committee (Proposal No. 2017G589 and 2019G579). The SANS experiment at the Materials and Life Science Experimental Facility of the J-PARC was performed under a user program (Proposal No. 2018B0265). The authors thank Prof. Hajime Ito (Hokkaido University, Japan) for his assistance with the AFM experiments, Mr. Toshiaki Ito (Hokkaido University, Japan) for his assistance with the TEM experiments, and Dr. Hiroki Iwase (CROSS, Japan) for his assistance with the SANS experiments.

Notes and references

1. M. Neisser and S. Wurm, *Adv. Opt. Technol.*, 2015, **4,** 235.
2. T. Ito and S. Okazaki, *Nature*, 2000, **406,** 1027.
3. L. Li, X. Liu, S. Pal, S. Wang, C. K. Ober and E. P. Giannelis, *Chem. Soc. Rev.*, 2017, **46,** 4855.
4. M. P. Stoykovich and P. F. Nealey, *Mater. Today*, 2006, **9,** 20.
5. M. Li and C. K. Ober, *Mater. Today*, 2006, **9,** 30.
6. S. -J. Jeong, J. Y. Kim, B. H. Kim, H. -S. Moon and S. O. Kim, *Mater. Today*, 2013, **16,** 468.
7. K. Koo, H. Ahn, S. -W. Kim, D. Y. Ryu and T. P. Russell, *Soft Matter*, 2013, **9,** 9059.
8. C. M. Bates, M. J. Maher, D. W. Janes, C. J. Ellison and C. G. Willson, *Macromolecules*, 2014, **47,** 2.
9. M. D. Rodwogin, C. S. Spanjers, C. Leighton and M. A. Hillmyer, *ACS Nano*, 2010, **4,** 725.
10. Y. Luo, D. Montarnal, S. Kim, W. Shi, K. P. Barteau, C. W. Pester, P. D. Hustad, M. D. Christianson, G. H. Fredrickson, E. J. Kramer and C. J. Hawker, *Macromolecules*, 2015, **48,** 3422.
11. J. D. Cushen, I. Otsuka, C. M. Bates, S. Halila, S. Fort, C. Rochas, J. A. Easley, E. L. Rausch, A. Thio, R. Borsali, C. G. Willson and C. J. Ellison, *ACS Nano*, 2012, **6,** 3424.
12. J. Kwak, A. K. Mishra, J. Lee, K. S. Lee, C. Choi, S. Maiti, M. Kim and J. K. Kim, *Macromolecules*, 2017, **50,** 6813.

13. W. Zhang, M. Huang, S. al Abdullatif, M. Chen, Y. Shao-Horn and J. A. Johnson, *Macromolecules*, 2018, **51,** 6757.
14. P. Mansky, Y. Liu, E. Huang, T. P. Russell and C. Hawker, *Science*, 1997, **275,** 1458.
15. C. M. Bates, T. Seshimo, M. J. Maher, W. J. Durand, J. D. Cushen, L. M. Dean, G. Blachut, C. J. Ellison and C. G. Willson, *Science*, 2012, **338,** 775.
16. S. Kim, H. S. Wang, Y. Choe, S. H. Choi and J. Bang, *Polym. J.*, 2016, **48,** 33.
17. R. Nakatani, H. Takano, A. Chandra, Y. Yoshimura, L. Wang, Y. Suzuki, Y. Tanaka, R. Maeda, N. Kihara, S. Minegishi, K. Miyagi, Y. Kasahara, H. Sato, Y. Seino, T. Azuma, H. Yokoyama, C. K. Ober and T. Hayakawa, *ACS Appl. Mater. Interfaces*, 2017, **9,** 31266.
18. W. Lee, Y. Kim, S. Jo, S. Park, H. Ahn and D. Y. Ryu, *ACS Macro Lett.*, 2019, **8,** 519.
19. C. Tang, E. M. Lennon, G. H. Fredrickson, E. J. Kramer and C. J. Hawker, *Science*, 2008, **322,** 429.
20. H. K. Choi, J. Gwyther, I. Manners and C. A. Ross, *ACS Nano*, 2012, **6,** 8342.
21. S. H. Han, V. Pryamitsyn, D. Bae, J. Kwak, V. Ganesan and J. K. Kim, *ACS Nano*, 2012, **6,** 7966.
22. W. Shi, A. L. Hamilton, K. T. Delaney, G. H. Fredrickson, E. J. Kramer, C. Ntaras, A. Avgeropoulos and N. A. Lynd, *J. Am. Chem. Soc.*, 2015, **137,** 6160.
23. M. Huang, K. Yue, J. Huang, C. Liu, Z. Zhou, J. Wang, K. Wu, W. Shan, A. -C. Shi and S. Z. D. Cheng, *ACS Nano*, 2018, **12,** 1868.
24. T. Y. Lo, M. R. Krishnan, K. -Y. Lu and R. -M. Ho, *Prog. Polym. Sci.*, 2018, **77,** 19.
25. J. G. Son, K. W. Gotrik and C. A. Ross, *ACS Macro Lett.*, 2012, **1,** 1279.
26. G. M. Grason and R. D. Kamien, *Macromolecules*, 2004, **37,** 7371.
27. D. Mecerreyes, V. Lee, C. J. Hawker, J. L. Hedrick, A. Wursch, W. Volksen, T. Magbitang, E. Huang and R. D. Miller, *Adv. Mater.*, 2001, **13,** 204.
28. E. Harth, B. Van Horn, V. Y. Lee, D. S. Germack, C. P. Gonzales, R. D. Miller and C. J. Hawker, *J. Am. Chem. Soc.*, 2002, **124,** 8653.
29. A. R. De Luzuriaga, N. Ormategui, H. J. Grande, I. Odriozola, J. A. Pomposo and I. Loinaz, *Macromol. Rapid Commun.*, 2008, **29,** 1156.
30. B. Zhu, J. Ma, Z. Li, J. Hou, X. Cheng, G. Qian, P. Liu and A. Hu, *J. Mater. Chem.*, 2011, **21,** 2679.
31. B. T. Tuten, D. Chao, C. K. Lyon and E. B. Berda, *Polym. Chem.*, 2012, **3,** 3068.
32. A. Sanchez-Sanchez, A. Arbe, J. Colmenero and J. A. Pomposo, *ACS Macro Lett.*, 2014, **3,** 439.
33. P. G. Frank, B. T. Tuten, A. Prasher, D. Chao and E. B. Berda, *Macromol. Rapid Commun.*, 2014, **35,** 249.
34. N. Hosono, M. A. J. Gillissen, Y. Li, S. S. Sheiko, A. R. A. Palmans and E. W. Meijer, *J. Am. Chem. Soc.*, 2013, **135,** 501.
35. I. Perez-Baena, I. Asenjo-Sanz, A. Arbe, A. J. Moreno, F. L. Verso, J. Colmenero and J. A. Pomposo, *Macromolecules*, 2014, **47,** 8270.
36. K. Watanabe, R. Tanaka, K. Takada, M. -J. Kim, J. -S. Lee, K. Tajima, T. Isono and Toshifumi Satoh, *Polym. Chem.*, 2016, **7,** 4782.
37. R. Tanaka, K. Watanabe, T. Yamamoto, K. Tajima, T. Isono and T. Satoh, *Polym. Chem.*, 2017, **8,** 3647.
38. K. Watanabe, S. Katsuhara, H. Mamiya, T. Yamamoto, K. Tajima, T. Isono and T. Satoh, *Chem. Sci.*, 2019, **10,** 3330.
39. A. S. Zalusky, R. Olayo-Valles, J. H. Wolf and M. A. Hillmyer, *J. Am. Chem. Soc.*, 2002, **124,** 12761.
40. I. Keen, A. Yu, H. -H. Cheng, K. S. Jack, T. M. Nicholson, A. K. Whittaker and I. Blakey, *Langmuir*, 2012, **28,** 15876
41. D. Mecerreyes, V. Lee, C. J. Hawker, J. L. Hedrick, A. Wursch, W. Volksen, T. Magbitang, E. Huang and R. D. Miller, *Adv. Mater.*, 2001, **13**, 204.
42. I. Vukovic, T. P. Voortman, D. H. Merino, G. Portale, P. Hiekkataipale, J. Ruokolainen, G. ten Brinke and K. Loos, *Macromolecules*, 2012, **45,** 3503.
43. B. Goderis, H. Reynaers, M. H. Koch and V. B. F. Mathot, *J. Poly. Sci. Part B: Polym. Phys.* 1999, **37**, 1715.
44. L. Han, G. Shan, Y. Bao and P. Pan, *J. Phys. Chem. B*, 2015, **119**, 14270.
45. I. W. Hamley and V. Castelletto, *Prog. Polym. Sci.*, 2004, **29,** 909.
46. G. M. Grason, *Phys. Rep.*, 2006, **433,** 1.
47. I. Teraoka, *Polymer Solutions: An Introduction to Physical Properties*, John Wiley & Sons, New York, 2002.
48. Although we had prepared the thin film of $S_{65}BS_{28}(cl)$–LA_{459} and $S_{47}BS_{47}(cl)$–LA_{484} on Si substrates modified with the PS-*r*-PMMA of different compositions as well as PMMA underlayer, the perpendicular orientation could not be achieved most likely due to the high polarity of the BCPs.
49. A. Baruth, M. D. Rodwogin, A. Shankar, M. J. Erickson, M. A. Hillmyer and C. Leighton, *ACS Appl. Mater. Interfaces*, 2011, **3,** 3472.
50. A. Baruth, M. Seo, C. H. Lin, K. Walster, A. Shankar, M. A. Hillmyer and C. Leighton, *ACS Appl. Mater. Interfaces*, 2014, **6,** 13770.
51. X. Li, Y. Liu, L. Wan, Z. Li, H. Suh, J. Ren, L. E. Ocola, W. Hu, S. Ji and P. F. Nealey, *ACS Macro Lett.*, 2016, **5,** 396.
52. I. Keen, H. -H. Cheng, A. Yu, K. S. Jack, T. R. Younkin, M. J. Leeson, A. K. Whittaker and I. Blakey, *Macromolecules*, 2014, **47,** 276.